



JOINT INSTITUTE FOR NUCLEAR RESEARCH
Flerov Laboratory for Nuclear Reactions

FINAL REPORT ON THE START PROGRAMME

*IRRADIATION TESTING OF NUCLEAR
CERAMICS AND OXIDES WITH HEAVY
IONS OF FISSION FRAGMENTS
ENERGIES*

Supervisor:

Dr. V.A Skuratov

Student:

Madeleine Badenhorst,
South Africa,
Nelson Mandela University

Participation period:

July 21 – September 14,
Summer Session 2024
Dubna, 2024

TABLE OF CONTENTS

Abstract	2
1. Introduction	2
2. Literature Review	3
2.1 SHI Irradiation Fundamentals: Dense Ionization and Phase Transformations.....	3
2.2 Overview of CeO ₂ and YIG: Nuclear Ceramic and Ferrimagnetic Materials.....	4
3. Experimental Procedure	4
4. Results and Discussion	5
5. Conclusion	18
6. Acknowledgements	19
References	19

Abstract

In this study, the transmission electron microscopy (TEM) technique was utilised to investigate the effect of swift heavy ion (SHI) irradiation on both yttrium iron garnet (YIG), $Y_3Fe_5O_{12}$, and ceric oxide, CeO_2 nanocrystals. The specimens were irradiated with bismuth (Bi), xenon (Xe) and krypton (Kr) ions with energies ranging from 148 to 714 MeV to fluences between $2 \times 10^{11} \text{ cm}^{-2}$ to $5 \times 10^{12} \text{ cm}^{-2}$ with and without different thickness aluminium degraders. The typical electronic stopping powers were between 11 and 41 keV/nm. Unfortunately, due to limitations such as contamination and defocus, a reduced data set was analysed. The tracks as well as the nanoparticle size distributions were graphically represented through ImageJ and OriginPro software. Amorphous tracks were observed for nanocrystal YIG specimens, whereas in CeO_2 nanocrystals, the crystal structure was retained, despite irradiation. Thus, CeO_2 is a possible candidate material to be used as an inert matrix fuel host. This study illustrates the different radiation responses of these two materials and the results could assist with the development of radiation-resistant nanomaterials.

1. Introduction

The economy of a country is strongly dependent on the capability of energy production. Clean, reliable energy is necessary to reduce climate change and the predicted exhaustion of fossil fuel encourages the implementation of nuclear power to deliver clean energy [1]. It was reported by S. J. Zinkle and G. S. Was in 2013 that 66 % of worldwide greenhouse gas emissions originate from fossil fuels and nuclear energy emits a limited amount of greenhouse gas due to its very low carbon emissions [2]. The escalating energy crisis encouraged recent studies in advancing nuclear reactor materials to solve the radiation stability problems of inert matrix fuel hosts and coated fuel particles [1]. Materials used for nuclear energy systems must operate at extreme conditions such as high temperatures, survive high displacements per atom (dpa), and must withstand corrosive environments [3]. The type of radiation will induce a specific kind of damage, namely neutron exposure induces displacement damage, gamma and beta radiations induce ionisation and heating, whereas self-irradiation from alpha-decay, as well as fission fragments, induces structural defects [2,4]. These induced damages will result in the degradation of the material properties and lead to failure or reduced efficiency in nuclear systems. The conditions of materials exposed to fission fragments in nuclear reactors can be simulated with SHIs [5]. Therefore it is vital to understand SHI-induced damage within materials [5]. Irradiation experiments involving SHIs are a relatively unexplored topic [6]. This is attributed to the inability to investigate their effects with classical low-energy ion implanters [6].

In this study, the structural defects induced by SHIs with energies above 1 MeV/amu within the nuclear ceramic material, nanocrystal CeO_2 , as well as within the ferrimagnetic material, nanocrystal YIG, are investigated through the implementation of TEM for characterisation. It is essential to differentiate between nanocrystalline and nanocrystals. Nanocrystalline refers to a bulk polycrystalline material which consists of crystallites where the dimensions are in the nanometer range. While nanocrystals denote individual crystals with sizes in the nanoscale region. Throughout this study, the term nanocrystals will be used, emphasizing the focus on single, nano-sized crystals. Furthermore, this study provides a quantitative analysis of SHI track size as a function of ion energy and particle size.

2. Theory

2.1 SHI Irradiation Fundamentals: Dense Ionisation and Phase Transformations

SHIs have kinetic energy and mass greater than 1 MeV/amu and 10 amu respectively and are produced at large accelerator facilities [5]. There is considerable practical and theoretical interest in their interaction with solid targets since the mass-energy combinations are common in fission fragments and cosmic radiation [5]. The damage induced in a crystal by low (slow) - and high (swift heavy) -energy ions is depicted in Fig. 1 [7].

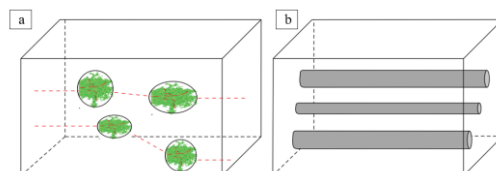


Fig. 1. Radiation damage configuration induced by (a) slow, low-energy ions and (b) swift, high-energy ions in irradiated crystals [7]

Fig. 1 (a) illustrates green-stained features corresponding to defect sites induced by the interaction between slow ions, with energy below 10 keV/amu, and the target atoms [7]. Their trajectories, shown by red dotted lines, are altered with each interaction as it transfers energy to the atoms through elastic collisions and its energy loss per unit distance is denoted as the nuclear stopping power (S_n) [7]. These interactions lead to the displacement of target atoms and then subsequent displacement of the other target atoms through several secondary and higher-order collisions [7]. In contrast, cylindrical shapes are shown in Fig. 1 (b), which represents the interactions between the SHIs and the material [7]. The nanometer-sized, cylindrical tracks are produced when the SHI passes through the material, up to hundreds of microns in depth, with target atoms and electrons assumed frozen in space [8]. The target electrons are excited by the ions within a few angstroms around its path [8]. This is attributed to the energy deposition from the ions to the target electrons primarily through excitation and ionisation processes and the ion energy loss per unit distance is denoted as the electronic stopping power (S_e). This results in the cascade of dense electronic excitations and ionisations of the target atoms [5]. Delta electrons generate cascades of secondary electrons as they propagate outward from the SHI trajectory and transfer energy to the lattice within picoseconds through electron-phonon coupling [8]. Therefore, high energy densities are expected which leads to the material heating up rapidly within picoseconds over a nanoscale region surrounding the cylindrical track, typically with a diameter from one to ten nanometers [8]. A thermal spike is observed during this interaction and there is a possibility of localised melting and subsequent rapid quenching [8]. More than 95 % of the energy transfer is attributable to the electronic ion energy losses in contrast to the energy deposition to the target atoms which is considered negligible along the SHI trajectory with the exception near the end of the ion range [8].

Theoretical models are used to describe the electronic kinetics after initial excitation and subsequent energy transfer of the SHIs to the target material [5]. Molecular dynamics (MD) simulations are used to study the resultant damage induced by dense ionisations during SHI-target interactions [5]. However, due to computational time restraints, this approach is a simplified approximation [5]. Simple estimations of the required parameters, such as the track radii, can be obtained using some

models provided adjustable parameters are defined [5]. One of these models includes the inelastic thermal spike (i-TS) model which describes the track formations by transient thermal processes for a cylindrical geometry [5, 9]. This model is based on two equations for thermal diffusion in the electron and atom subsystems coupled via the electron-phonon coupling parameter [5]. Alternatively, the Coulomb explosion mechanism, described by Gibbons and other models, can be employed to describe these interactions as well as other damage buildup [5, 7]. These models will not be discussed in this study but for additional in-depth analysis, the reader is directed to studies from M. Lang et al. [5] and L. Thomé et al. [7].

2.2. Overview of CeO₂ and YIG: Nuclear Ceramic and Ferrimagnetic Materials

Nuclear ceramic materials are used for various purposes including radioactive waste management and as inert matrix fuel hosts for actinide transmutation [7]. Inert matrix fuel hosts ensure a stable, durable structure that is able to withstand extreme radiation and temperature conditions [10]. This improves the safety and performance of nuclear fuel by mitigating the release of fission products and aiding in the transmutation of minor actinides [10]. Their selection is based on certain criteria such as high melting point, low thermal neutron absorption cross-section, high conductivity, good mechanical behaviour, thermal and radiation stability as well as compatibility with reactor coolant and cladding [10]. CeO₂ is a nuclear ceramic material which exhibits excellent thermal, chemical and radiation resistance properties [7]. When irradiated with SHIs a complex behaviour is observed with atomic-scale defects that alter its microstructure, chemistry and material properties [11]. This material is deemed as a candidate for an inert matrix fuel host for the transmutation of minor actinides [11]. At ambient conditions, this oxide ceramic has a fluorite structure which displays excellent resistance to high-energy particle irradiations [12]. This material is well-studied as a surrogate material for investigating the radiation effects of uranium dioxides due to its identical crystal structure and common properties [12]. It was observed in previous studies that continuous ion tracks are formed when $S_e > 15$ keV/nm in CeO₂ when irradiated with SHIs [12]. The oxide ceramic maintains its crystal structure after irradiation to high fluences as characterised by TEM [12].

In contrast, YIG is a ferrimagnetic material used for data storage devices, which exhibits a garnet structure, with cubic symmetry and magnetic properties [13]. The damage induced by SHI irradiations in magnetic oxides, particularly YIG, in the electronic stopping power regime has been researched for several years [13]. This is attributed to the characteristic amorphous tracks produced in YIG above its threshold electronic stopping power S_e [13]. As well as its unique properties such as exceptional responses at high-frequency electromagnetic waves and stability under thermal stress [13].

3. Experimental Procedure

In this study commercial nanocrystals (nc) YIG and CeO₂ powder specimens were purchased from Sigma-Aldrich. Prior to the irradiation experiment, specimens were prepared for TEM analysis. All specimens were prepared in a similar manner but with different parameters for centrifugation. The nanopowder was weighed and then ground in an agate mortar and pestle. Thereafter, the ground powder was placed in a test tube and mixed with an organic solvent, either ethanol or hexane. The mixture was dispersed using an ultrasonic bath for about fifteen to thirty minutes and the amplitude of the ultrasonic waves was set to about 20 %. After ultrasonic treatment, a centrifuge was used to

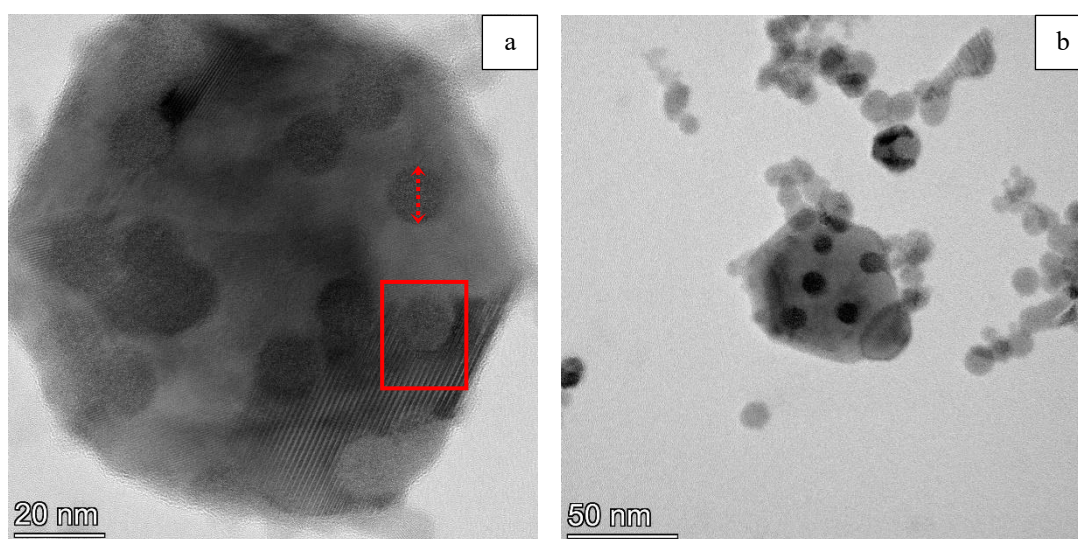
perform sedimentation, separating particles into fractions. The irradiation experiments and TEM analysis were conducted on the dispersed specimens which were placed on TEM copper grids.

The IC-100, and U-400 cyclotrons at FLNR JINR (Dubna, Russia), and DC-60 cyclotron at Astana Branch of Institute of Nuclear Physics (Nur-Sultan, Kazakhstan) were used to irradiate the specimens at room temperature. The nc-CeO₂ specimens were irradiated with 714 MeV Bi, 100 MeV Kr, and 148, 156, 167, and 220 MeV Xe ions to fluences of $5 \times 10^{11} \text{ cm}^{-2}$ to $5 \times 10^{12} \text{ cm}^{-2}$. The nc-YIG specimens were irradiated with 670 MeV Bi, 230 and 475 MeV Xe ions to fluences of $2 \times 10^{11} \text{ cm}^{-2}$ to $5 \times 10^{12} \text{ cm}^{-2}$. Aluminium (Al) degraders of thicknesses, ranging from 7.5 μm to 36.4 μm , were used to alter the range of energy of the ions. SRIM code was used to calculate the S_e values as well as the energy spreading

A high-resolution Talos F200i S/TEM operating at 200 kV, was employed for structural analysis of the nanoparticles prior to and after the irradiation experiments. The image processing and analysis software, ImageJ Version 1.54j, and the data analysis and graphing software tool, OriginPro, were used to measure the track diameters observed in the dark-field (DF), bright-field (BF) and HRTEM images and graphically represent the respective track size distributions. This approach relies on the contrast between the tracks and the nanoparticles in the TEM images to discern the tracks as circular features with sharp boundaries. In practice, the track diameter measurements have some degree of uncertainty due to diffraction effects producing contrast unrelated to the ion tracks, especially for irregularly shaped tracks.

4. Results and Discussion

The study investigates the track sizes induced by high-energy ions in two different materials, namely nc-YIG and -CeO₂. Once the electronic stopping power exceeds a specific threshold value, ion tracks are formed from high-energy Xe and Bi ions. This is evident through the investigation of BF and DF TEM images of irradiated nc-YIG specimens by 670 MeV Bi, 475 MeV and 230 MeV Xe ions with different aluminium degraders as shown in Fig. 2.



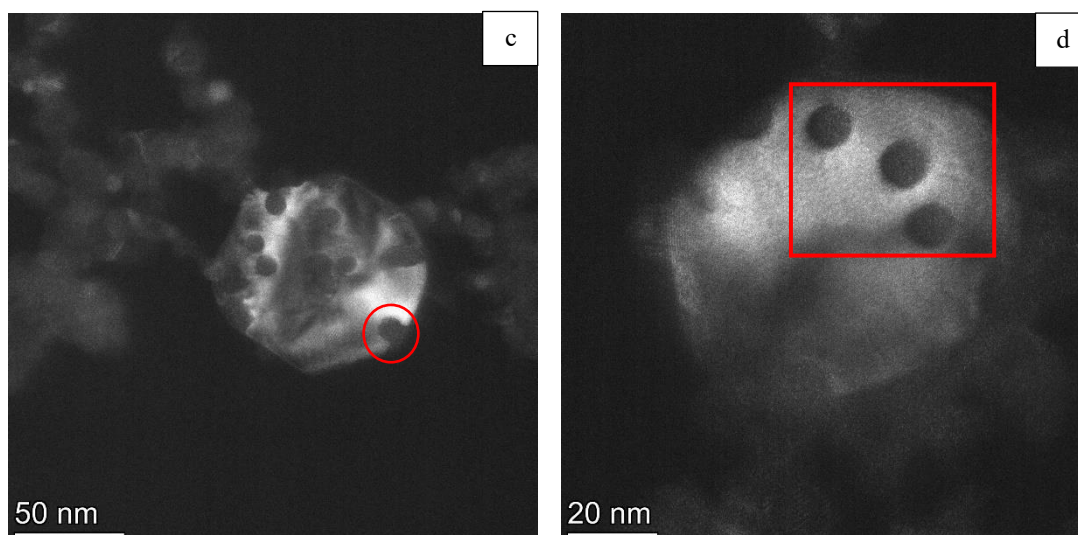


Fig. 2. BF TEM images of nc-YIG irradiated with (a) Bi ($S_e = 34.32 \pm 0.11$ keV/nm) and (b) Xe ($S_e = 26.64 \pm 0.04$ keV/nm) as well as DF TEM images irradiated with (c) Xe ($S_e = 25.61 \pm 0.11$ keV/nm), and (d) Xe ($S_e = 21.91 \pm 0.16$ keV/nm) ions, each to a fluence of 2×10^{11} cm $^{-2}$. The red dotted, bidirectional arrow represents a typical diameter measurement, the red boxes depict the contrast between an amorphous track and crystalline nanoparticle, and the red circle indicates the amorphous defects present at the border of the particles

It is clear from Fig. 2, that the morphology of the tracks appears circular, representing cross sections of the amorphous cylindrical ion tracks [14]. The tracks could be identified and distinguished from the nanoparticles due to their uniform intensities and the lack of diffraction contrast and lattice fringes inside their cores, as annotated by the red boxes in Fig. 2 (a) and (d). The track diameters were measured through the utilisation of the line tool in ImageJ, as depicted by the red dotted, bidirectional arrow in Fig. 2 (a) across the crystalline-amorphous boundary. To ensure consistency, only distinct, non-overlapping tracks were measured. From the DF images, Fig. 2 (c) and (d), the crystalline regions are perceived as bright regions. In contrast, due to their amorphous nature (absence of strong diffraction), the amorphous tracks are perceived as dark regions. As annotated by the red circle in Fig. 2 (c), it is evident that larger tracks are present near or on the border of the particles since it is thinner in projection than areas closer to the middle of the particle. Hence, these tracks on the borders of the particles were excluded from the measurements. Furthermore, degrader thicknesses of $36.4 \mu\text{m}$ ($S_e = 4.63 \pm 0.30$ keV/nm) for 670 MeV Bi ions and $30.5 \mu\text{m}$ and $33.8 \mu\text{m}$ ($S_e = 7.82 \pm 0.70$ keV/nm and $S_e = 2.82 \pm 0.43$ keV/nm respectively) for 475 MeV Xe ions, were also excluded due to the absence of visible tracks or the insufficient number of observable tracks. The nc-YIG specimens were also irradiated with 230 MeV Xe ions to a fluence of 2×10^{12} cm $^{-2}$ and 5×10^{12} cm $^{-2}$. However, at higher fluences there was a significant amount of track overlap, and a corresponding increase in uncertainty in determining the track borders. It was observed that the nanoparticles have become amorphous at these fluences due to the overlap of amorphous ion tracks.

The quality of the TEM images was influenced by factors such as defocus, astigmatism, and contamination. Therefore, the data set was reduced and only TEM images with high contrast and good focus were selected. BF imaging mode could impose some restrictions on differentiating between the tracks and the nanoparticles. BF imaging mode could be utilised as shown in Fig. 2 (b) as some tracks were clearly visible. However, it is suggested for future studies to base the track measurements on high-angular dark-field scanning transmission electron microscopy (HAADF STEM) images to enhance the contrast independent of the local diffraction condition and thus

improve the consistency of the measurements [15,16]. HAADF STEM imaging relies on the assumption that the specimen thickness and chemical composition are uniform, generally only valid for the small area within the field of view, and its contrast is related to the projected average atomic number of the specimen [15]. The current data sets provide a valuable understanding of track formations, however, their limitations are acknowledged.

The effect of ion energy was investigated through the generation of track size histograms for each irradiation case. These size distributions provide a visual representation of the measured track size dispersion and their respective population size. Histograms for nc-YIG with 670 MeV Bi, 475 MeV Xe, and 230 MeV Xe ions, both with and without Al degraders, are shown in Figs. 3, 4, and 5, respectively.

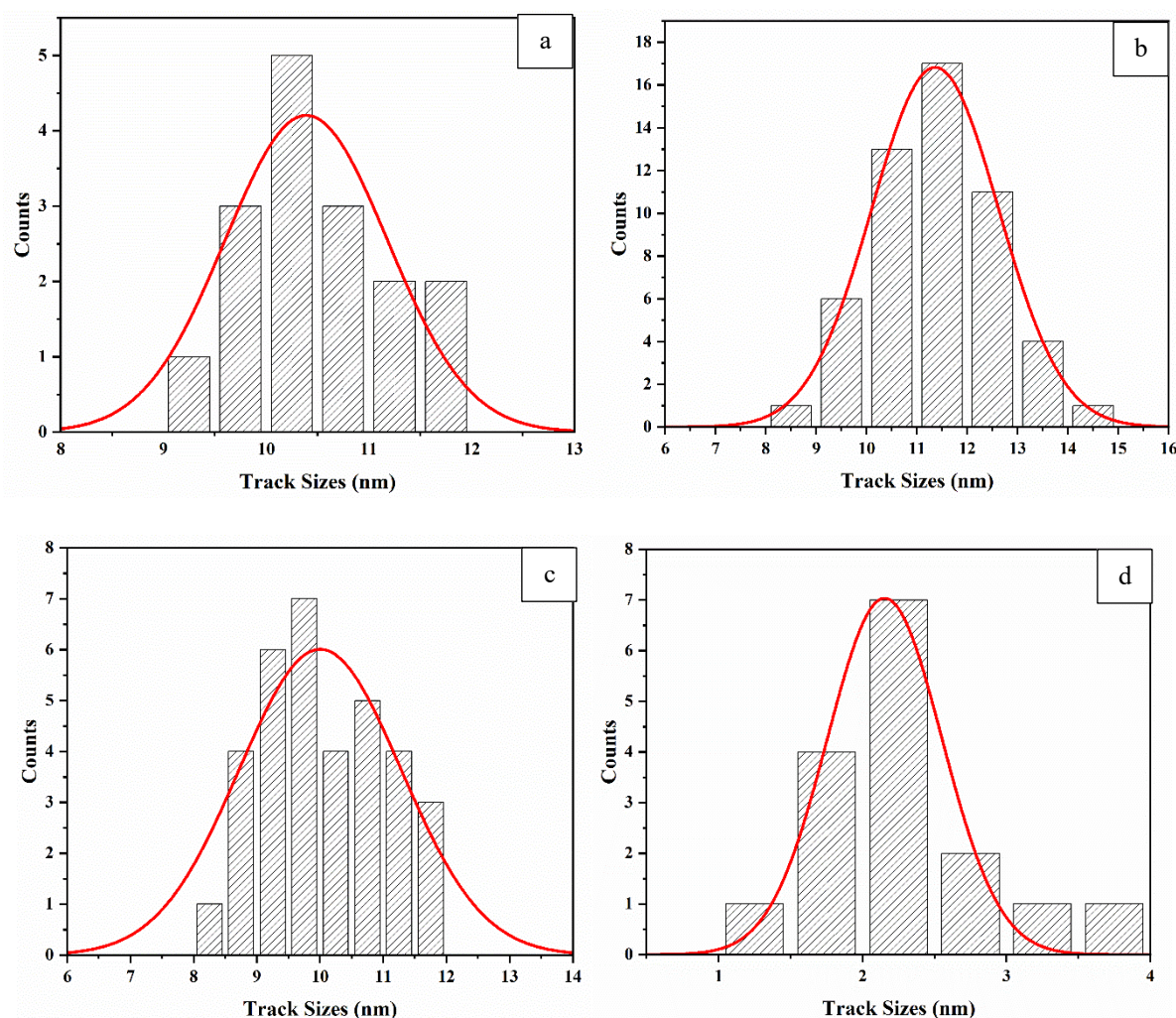


Fig. 3. Histograms of the track diameters for nc-YIG irradiated with 670 MeV Bi ions to a fluence of $2 \times 10^{11} \text{ cm}^{-2}$ (a) without an Al degrader, (b) with 15 μm , (c) 22 μm , and (d) 32.8 μm Al degraders. The size distributions were fitted with a Gaussian distribution as indicated by the red line.

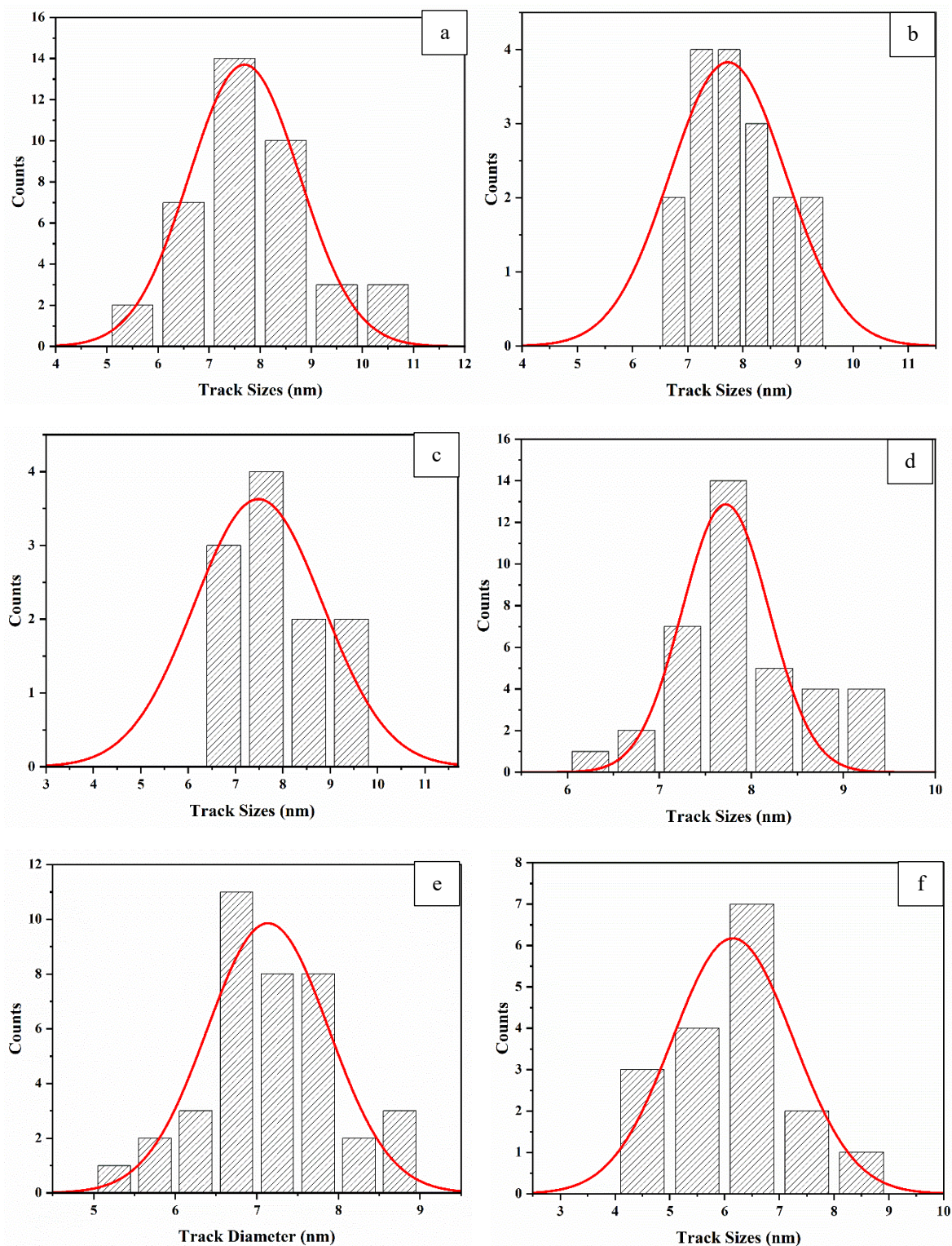


Fig. 4. Histograms of the track diameters for nc-YIG irradiated with 475 MeV Xe ions to fluence of $2 \times 10^{11} \text{ cm}^{-2}$ (a) without Al degrader, (b) with 13.6 μm , (c) 18.1 μm , (d) 22 μm , (e) 25.7 μm , and (f) 28.7 μm Al degraders. The size distributions were fitted with Gaussian as indicated by the dotted line.

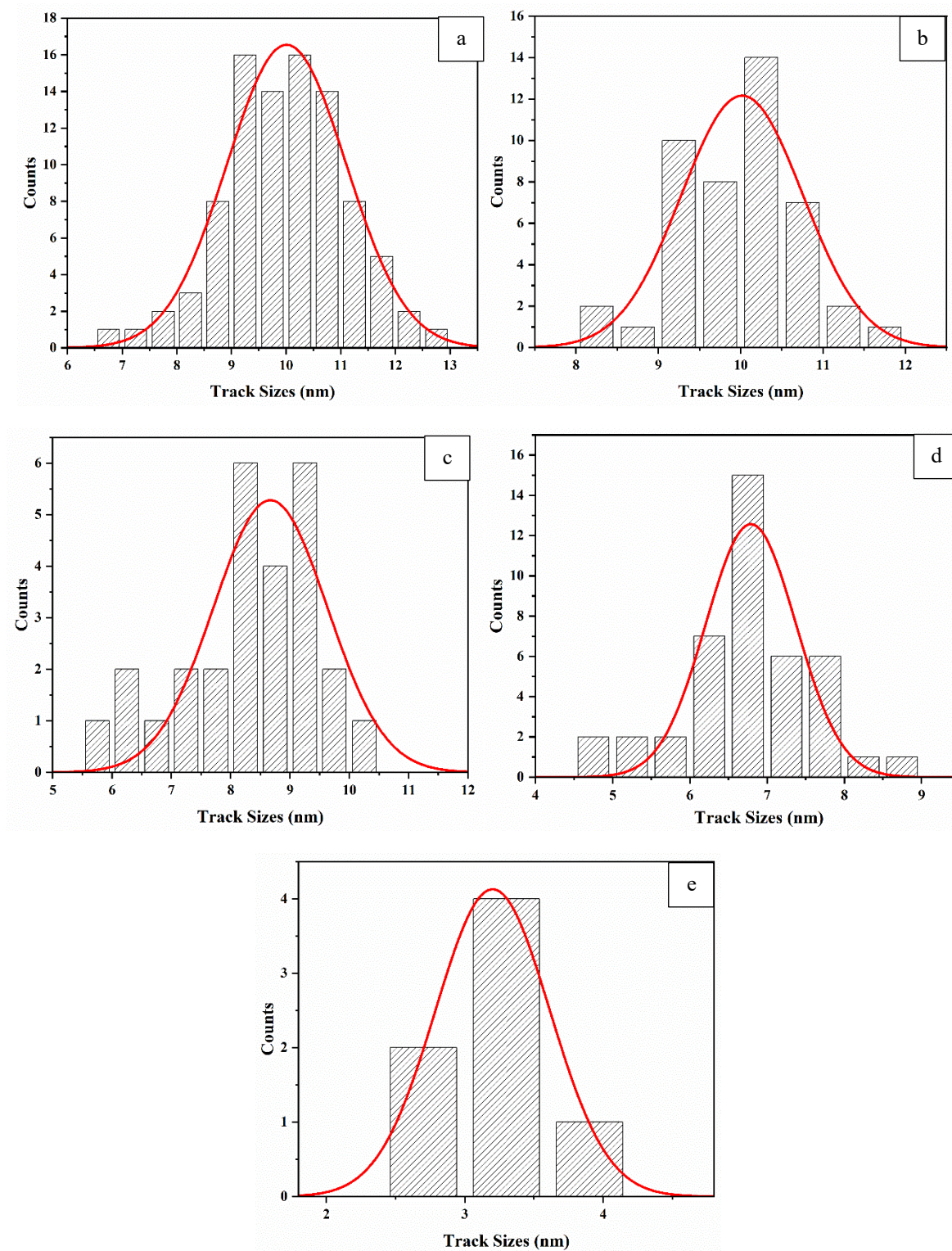


Fig. 5. Histograms of the track diameters for nc-YIG irradiated with 230 MeV Xe ions to a fluence of $2 \times 10^{11} \text{ cm}^{-2}$ (a) without Al degrader, (b) with 8 μm , (c) 11.7 μm , (d) 14 μm , and (e) 17 μm Al degraders. The size distributions were fitted with Gaussian as indicated by the red line.

OriginPro was used to generate the track size distributions and each plot was fitted with a Gaussian distribution from which the mean and standard deviation was extracted [17]. Figs. 3, 4 and 5 illustrate a high degree of variability as the track diameter measurements span a wide range of values.. The low number of counts is attributed to the exclusion of some of the TEM images and the exclusion of

poorly contrasting, overlapping, and near edge tracks. The track size distributions remain a valuable data set notwithstanding these limitations.

The results for the track measurements as well as the details of the irradiation parameters were tabulated in Table 1. These results include the initial ion energies, the thicknesses of Al degraders, and the extracted results from Figs. 3, 4 and 5. The S_e values were determined through SRIM-2016 and the density of YIG was considered as 5.17 g/cm^3 . The energy straggle of the incident ion beam after it traversed through the Al degrader. The energy dispersion of the initial ion beam was not considered.

Table 1

Summary of irradiation parameters, calculated electronic stopping powers with 2σ for 95 % confidence interval and extracted track parameters for nanocrystalline $\text{Y}_3\text{Fe}_5\text{O}_{12}$

Ion and Initial Energy (MeV)	Al Degradier Thickness (μm)	Ion Energy (MeV/amu)	Average $S_e \pm 2\sigma$ (keV/nm)	Mean (nm)	Standard Deviation (nm)	Min (nm)	Max (nm)	# of Tracks Measured
Bi, 670	None	3.2	41.19	10.39	0.79	9.06	11.85	16
	15.85 \pm 0.15	1.34 \pm 0.01	34.32 \pm 0.11	11.36	1.25	8.46	14.18	53
	22.05 \pm 0.22	0.76 \pm 0.01	27.43 \pm 0.17	10.00	1.28	8.48	11.79	34
	32.82 \pm 0.29	0.14 \pm 0.01	9.35 \pm 0.43	2.15	0.39	1.44	3.61	14
Xe, 475	None	3.59	28.94	7.69	1.08	5.64	10.96	39
	13.66 \pm 0.12	1.74 \pm 0.016	26.64 \pm 0.04	7.73	1.05	6.72	9.43	17
	18.10 \pm 0.21	1.44 \pm 0.03	25.61 \pm 0.11	7.48	1.36	6.43	9.82	11
	22.05 \pm 0.22	0.77 \pm 0.01	21.30 \pm 0.13	7.72	0.47	6.47	9.23	37
	25.77 \pm 0.28	0.43 \pm 0.03	16.69 \pm 0.55	7.14	0.74	5.42	8.99	38
	28.74 \pm 0.43	0.23 \pm 0.02	11.4 \pm 0.78	6.15	1.10	4.08	8.17	15
Xe, 230	None	1.74	26.66	10.00	1.06	6.87	12.64	91
	8.02 \pm 0.17	0.8 \pm 0.02	21.91 \pm 0.16	10.02	0.74	8.18	11.62	45
	11.74 \pm 0.25	0.47 \pm 0.02	17.51 \pm 0.37	8.67	0.96	5.98	10.08	27
	14.03 \pm 0.14	0.30 \pm 0.01	13.57 \pm 0.26	6.79	0.58	4.84	8.65	42
	17.4 \pm 0.19	0.12 \pm 0.01	6.92 \pm 0.36	3.20	0.41	2.41	4.09	7

It is expected that the track diameter should increase with increasing ion energy because higher energy ions will attribute to more energetic electrons and result in a broader distribution of energy depositions and consequently larger track diameters. However, while this is the general trend of the data, there are some outliers. track diameters are consistently larger for 230 MeV Xe ions than for the 475 MeV Xe ions at similar S_e (after degrader). This could be attributed to the reduced data set and previously discussed limitations for this investigation. Furthermore, the track measurements included the range, namely the maximum and minimum, in addition to the mean, standard deviation and number of tracks measured, which were tabulated in Table 1. The ranges provide a more comprehensive representation of the track size distribution as solely relying on the mean could result in misinterpretation of the variability and spread of the data. The thickness of the Al degrader foils were measured using a Mitutoyo Litematic VL-50 precision thickness gauge, which applies a

measuring force of 0.01 N. To ensure representative and reliable results, multiple measurements were taken for each degrader. Ten measurements were performed at different locations on each degrader, and the average value was calculated to represent the thickness. The standard deviation of these measurements was used to estimate the uncertainty associated with each thickness value.

In addition to the previous observations, the areas of the nanoparticles were determined in ImageJ through thresholding and the polygon selection tool. Fig. 6 represents the weighted size distributions of the nanoparticle areas for nc-YIG specimens irradiated with different irradiation conditions.

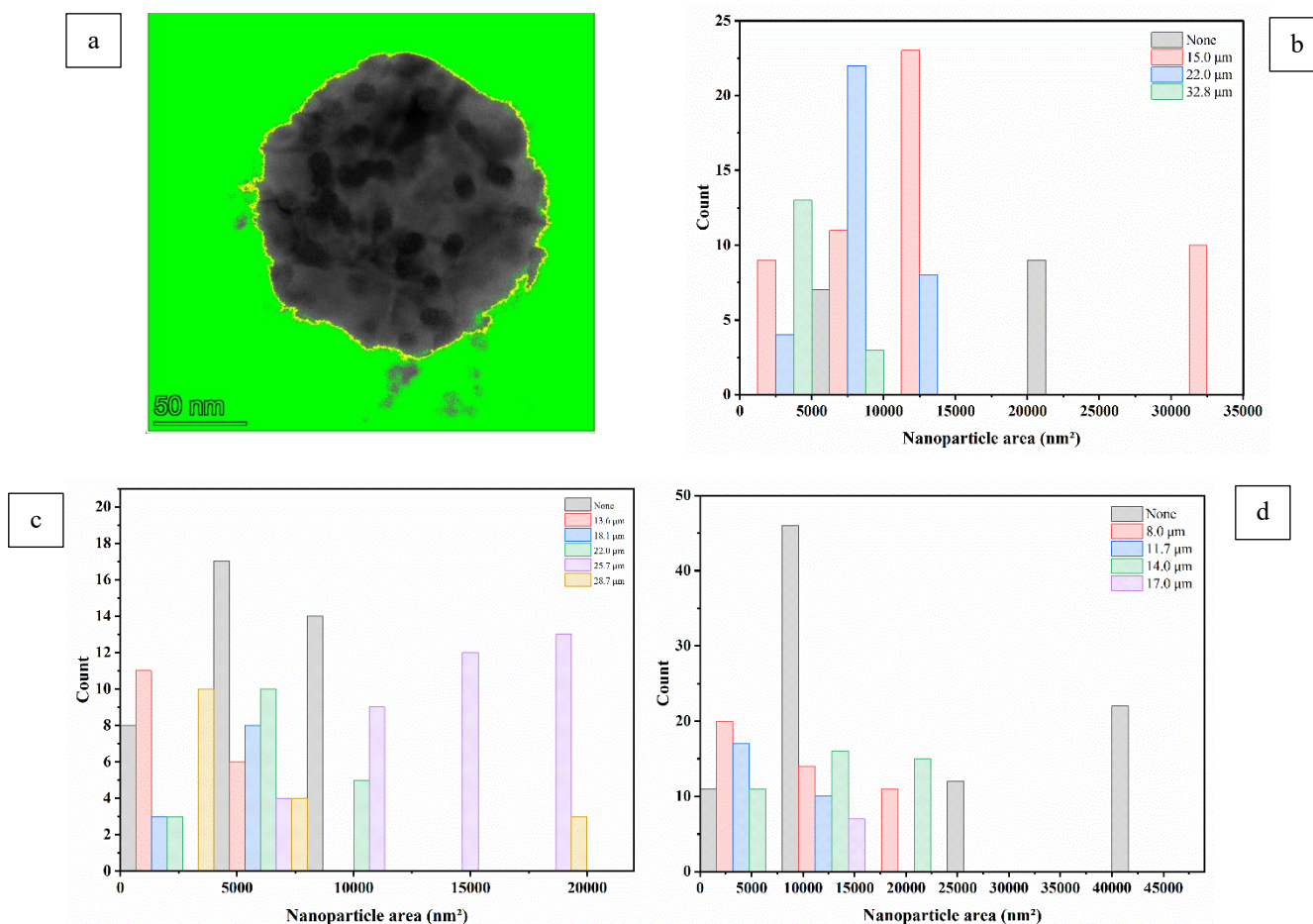


Fig. 6. (a) Nanoparticle area measurement via ImageJ thresholding and weighted nanoparticle area distribution illustrating track per area for irradiated nc-YIG specimens with (b) 670 MeV Bi, (c) 475 MeV Xe, and (d) 230 MeV Xe ions with different Al degrader thicknesses

Fig. 6 (a) indicates the thresholding, employed in ImageJ, which is represented by the green region. The BF and DF TEM images display distinct contrasts between nanoparticles which enables the use of the thresholding technique to determine the possible particle areas. Only particles where tracks could be measured were included in the data set. The number of tracks measured on the specific particle area was used to weight the area values in order to produce a dataset indicative of the number of samples obtained for a given grain size. The weighted distributions of the nanoparticle areas with measured tracks are shown in Fig. 6 (b) to (d). Typically, smaller particles exhibit larger tracks at lower S_e values [18]. Specific energy loss could vary significantly at different positions along the ion path for individual ions since the transfer of ion energy is a stochastic process [18].

The relationship between the average track diameters and the electronic stopping power, S_e , for all the irradiation conditions is graphically represented in Fig. 7.

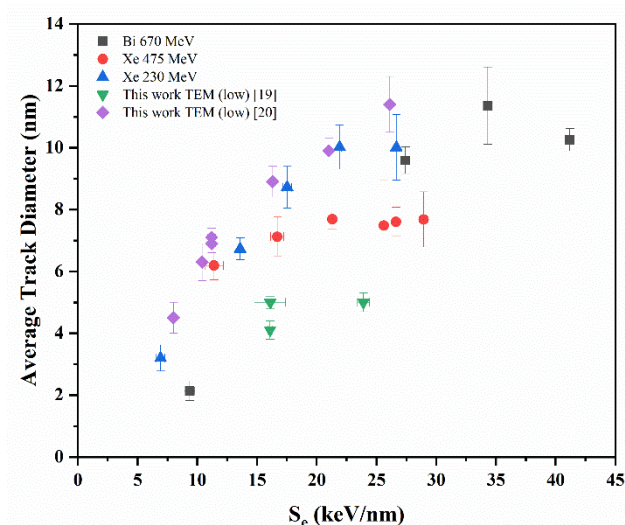
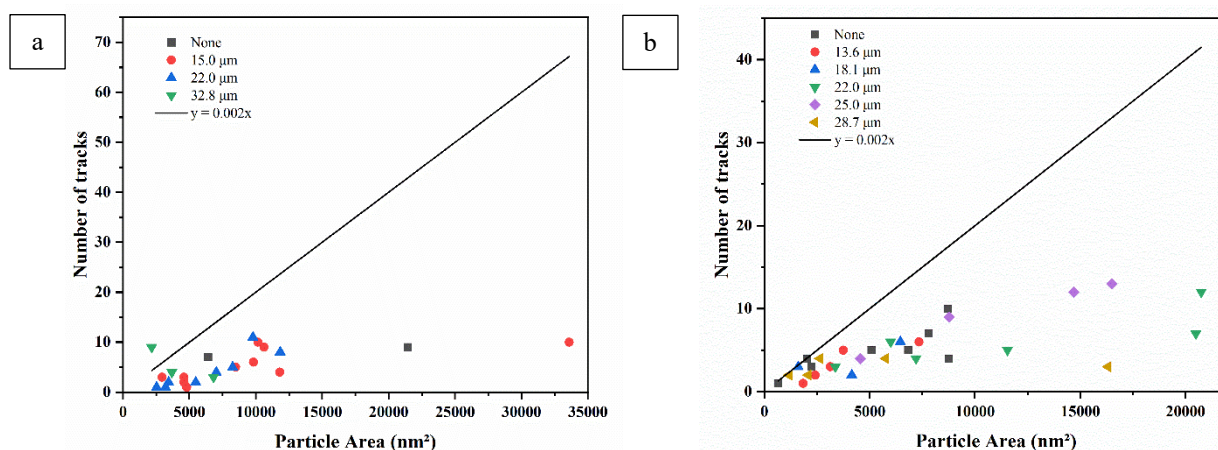


Fig. 7. Correlation between the average track diameter and electronic stopping power from the study and previous research on irradiated YIG specimens at low ion velocities [19, 20].

In Fig. 7, it is observed that the greater the electronic stopping power value, the greater the average track diameter, except for the last data point observed for 670 MeV Bi ions which displays a lower data point. Fig. 7 reveals that the results deviate from previous studies [19], but there is resemblance in shape between the data points for 230 MeV Xe ions and the data points from previous studies [20], which reported a positive correlation between amorphous track radii and electronic stopping power. Previous studies did not investigate Bi ions, and this study did not consider Kr ions for nc-YIG, making direct comparisons challenging due to different radiation conditions. The differences in the data points should not be attributed to the velocity effect since high-velocity ions were not investigated in this study.

Fig. 8 shows the number of tracks counted as a function of particle area.



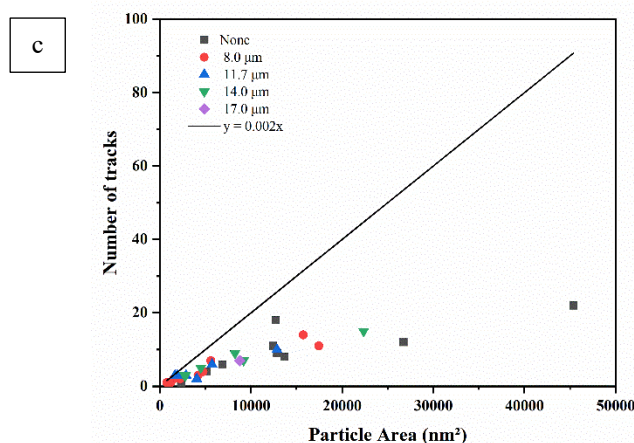
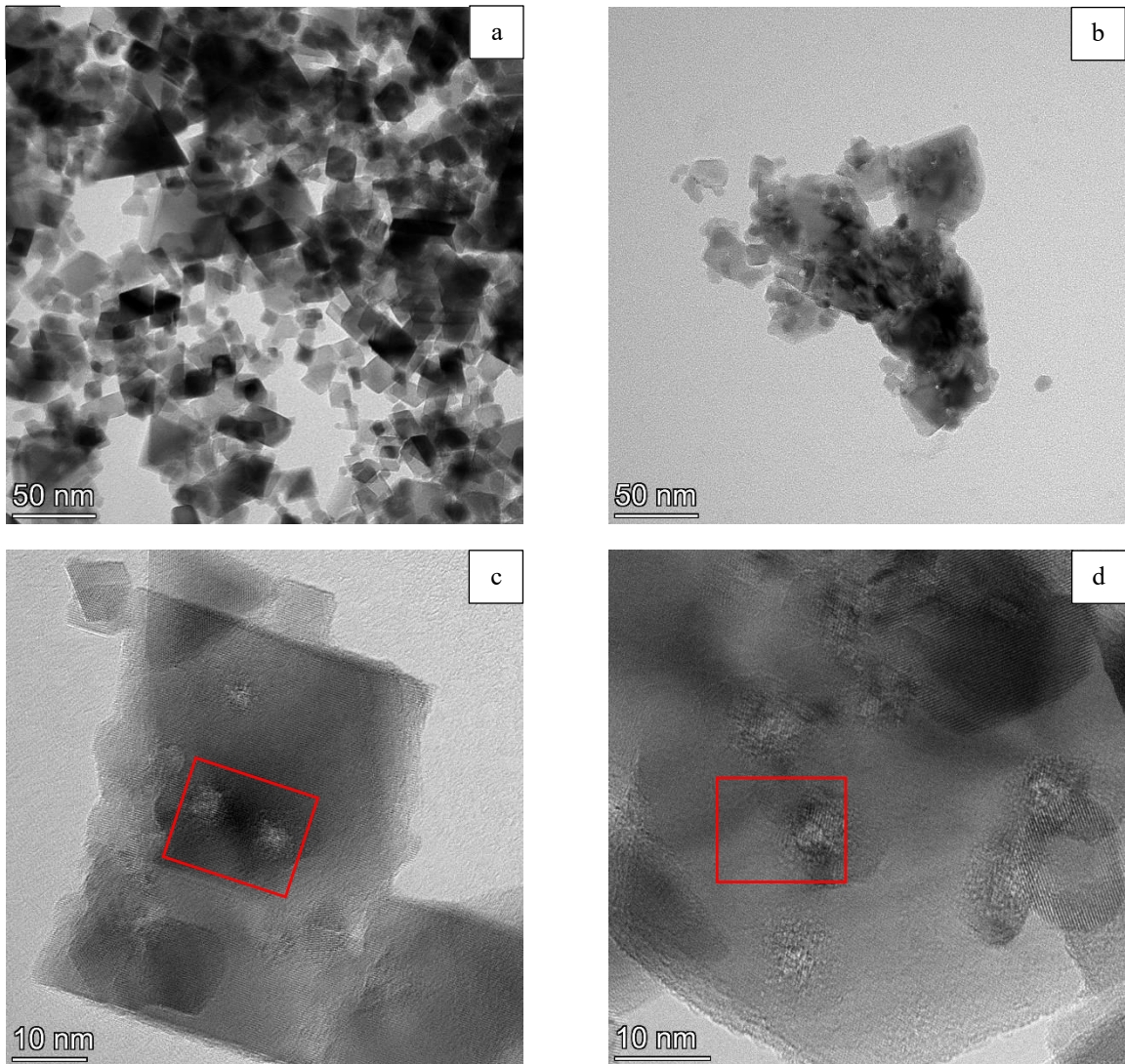


Fig. 8. Number of tracks versus particle area measured for nanocrystalline YIG irradiated with (a) 670 MeV Bi, (b) 475 MeV Xe and (c) 230 MeV Xe ions

It is shown in Fig. 8 that the expected slope of these curves would be the number of tracks per unit particle area, measured in nm^{-2} , which is of the applied fluence. Hence, the curve is described by the expression, $y = 0.002x$, which corresponds to $2 \times 10^{11} \text{ cm}^{-2}$. Deviations could be an indication of statistical fluctuations, errors in properly identifying tracks, disregarded tracks due to poor contrast or proximity to the particle edge, or variations in the efficiency of track creation. The latter is unlikely as the under sampling does not seem strongly correlated with S_e as it should be if tracks creation efficiency was responsible. It is seen in Fig. 8 that most of the data points lie below the theoretical line, except for one data point in Fig. 8 (a) representing the irradiation condition of 670 MeV Bi ions with the $32.8 \mu\text{m}$ Al degrader. This is most probably due to the small particle area. Adherence to the fluence line is a probabilistic phenomenon with increased probability for larger particles due to the random nature of ion impact coordinates. In Fig. 8 (b), four data points are found on the line which is an indication of sufficient sampling. The data points below the theoretical line suggest insufficient sampling of ion tracks in these particles to be completely representative. This means that the reliability of the data for these measurements is somewhat lower and better data is needed to draw reliable conclusions. There appears to be a systematic under sampling for larger particles. Assuming roughly spherical particles, particle areas of around 10000 nm^2 correspond to particles which are about 100 nm thick in the central region, tending to 0 thickness near the edges. This represents a significant change in target thickness which would result in track forming dynamics that are heavily surface biased near the edges of such a particle to mostly bulk biased near the centre. For lower S_e this could mean the difference between visible track creation near the edge and no track creation near the centre. The introduction of another parameter “fractional radius” defined as the normalised distance to the particle centre of mass would make for interesting analysis although the deviation from spherical particles in the current data set is significant and thus such a parameter would introduce high uncertainty. If the experiment would be repeated with HAADF images where image intensity could be related to local particle thickness, simultaneous analysis of the local thickness and track size would go a long way to reduce sampling inconsistencies. Overall data is expected to be below the fluence line due to filtering of neat edge tracks and poorly contrasting tracks. A compromise is needed between elimination of noisy data (edge tracks and poorly contrasting tracks) and the resulting increase in statistical noise due to fewer, and possible unrepresentative, samples. The plots suggest that the data reliability for larger particles are generally lower.

The track formations were also investigated in nc-CeO₂ irradiated with 714 MeV Bi ions to a fluence of $2 \times 10^{11} \text{ cm}^{-2}$, 100 MeV Kr ions to a fluence of $5 \times 10^{11} \text{ cm}^{-2}$, and 220, 167, 156 and 148 MeV Xe ions to fluences of $1 \times 10^{12} \text{ cm}^{-2}$ and $5 \times 10^{11} \text{ cm}^{-2}$, with and without Al degraders. Some of the BF, DF and HRTEM images of unirradiated and irradiated nc-CeO₂ specimens are shown in Fig. 9.



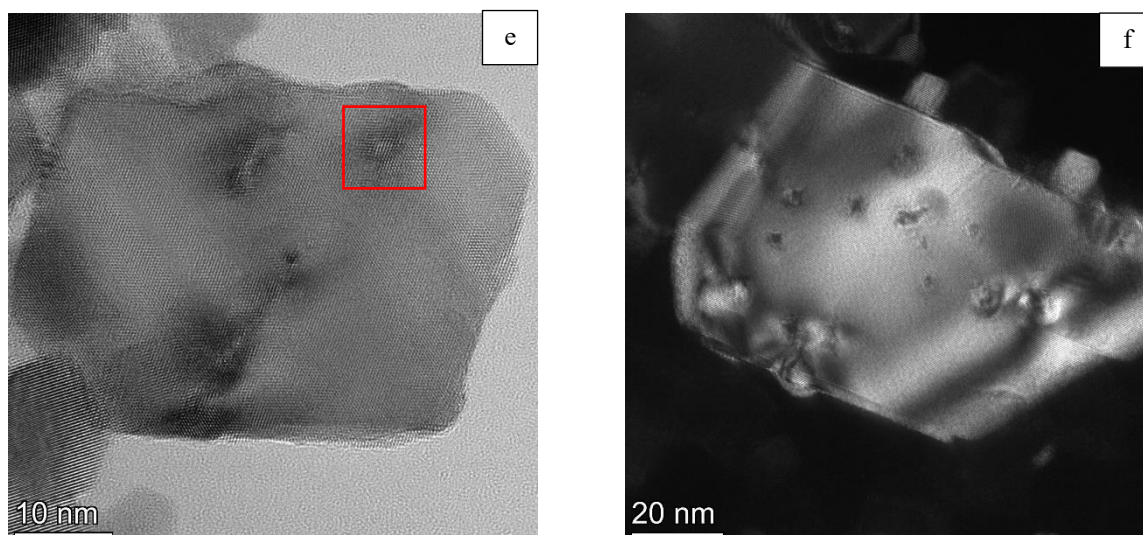


Fig. 9. (a) BF TEM image of unirradiated nc-CeO₂, and BF TEM images of nc-CeO₂ irradiated with (b) Xe ($S_e = 25.65$ keV/nm) ions to a fluence of 1×10^{12} cm⁻², and HRTEM TEM images of (c) Bi ($S_e = 22.58 \pm 0.53$ keV/nm), (d) Xe ($S_e = 16.11 \pm 0.26$ keV/nm), (e) Xe ($S_e = 27.66$ keV/nm), and a DF TEM image for irradiation with (f) Kr ($S_e = 21.45$ keV/nm) all to a fluence of 5×10^{11} cm⁻². The red boxes illustrate the tracks induced by the radiation and depict the fact that the crystalline structure still persists after penetration of the different high-energy ions

The nc-CeO₂ specimens were observed before and after irradiation in the TEM and the morphology and changes in the shapes of the nanoparticles were observed for both cases. Fig. 9 (a) depicts the unirradiated nanoparticles where the CeO₂ nanoparticles of cubic structure are primarily observed [21]. However, other morphologies are also observed such as nanorods and octahedrons with ambiguous triangular views [21]. Furthermore, a high amount of clustering of the nanoparticles is observed which minimises the surface area and is due to the high surface energy [21]. Overlapping nanoparticles are observed as darker regions in TEM analysis.

Through the comparison of Fig. 9 (a) and (b) to (f), it is observed that the nanoparticles maintain their cubic shape, however the edges appear more rounded. During analysis, it was observed that an increased fluence resulted in a greater change in shape around the edges. This is attributed to the radiation damage induced by the high-energy ions. CeO₂ has a fluorite-type structure and as discussed previously, has an excellent resistance to irradiation with energetic particles [12]. Previous investigations involving analysis with the TEM [22] and X-ray diffraction [23], concluded that CeO₂ maintains its crystal structure after irradiation with SHIs to high fluences, with a wide range of S_e up to about 30 keV/nm [22, 23]. However, surface hillocks are readily formed due to ion impact and is responsible for the observed rounding of particle edges. These investigations are supported by Fig. 9 (c) to (e) as indicated by the red boxes. The ion induced tracks observed have different contrasts compared to the nanoparticles and do not always appear circular. The TEM images shown in Fig. 2 for nc-YIG, illustrated amorphous tracks, whereas the tracks seen in Fig. 9 are not amorphous but retain its lattice structure. This observation is consistent with bulk CeO₂ irradiated with different ions. Studies involving defect formations induced by SHIs in CeO₂ are limited [12]. The tracks were measured using the same approach as for Fig. 2 (a), with the red dotted, bidirectional arrow in ImageJ. Irregular shapes and the overlapping and clustering of tracks impacted the accuracy of the track measurements. Furthermore the fact that tracks were still crystalline meant that a clear amorphous-crystalline boundary was not available to define the tracks and the measured size was highly

dependent on the local crystal orientation and diffraction condition (diffraction contrast). The track size distributions were utilised to extract the parameters presented in Table 2. The distribution curves for the selected nanoparticles are presented in Fig. 10. These histograms illustrate significant variability in track size measurements.

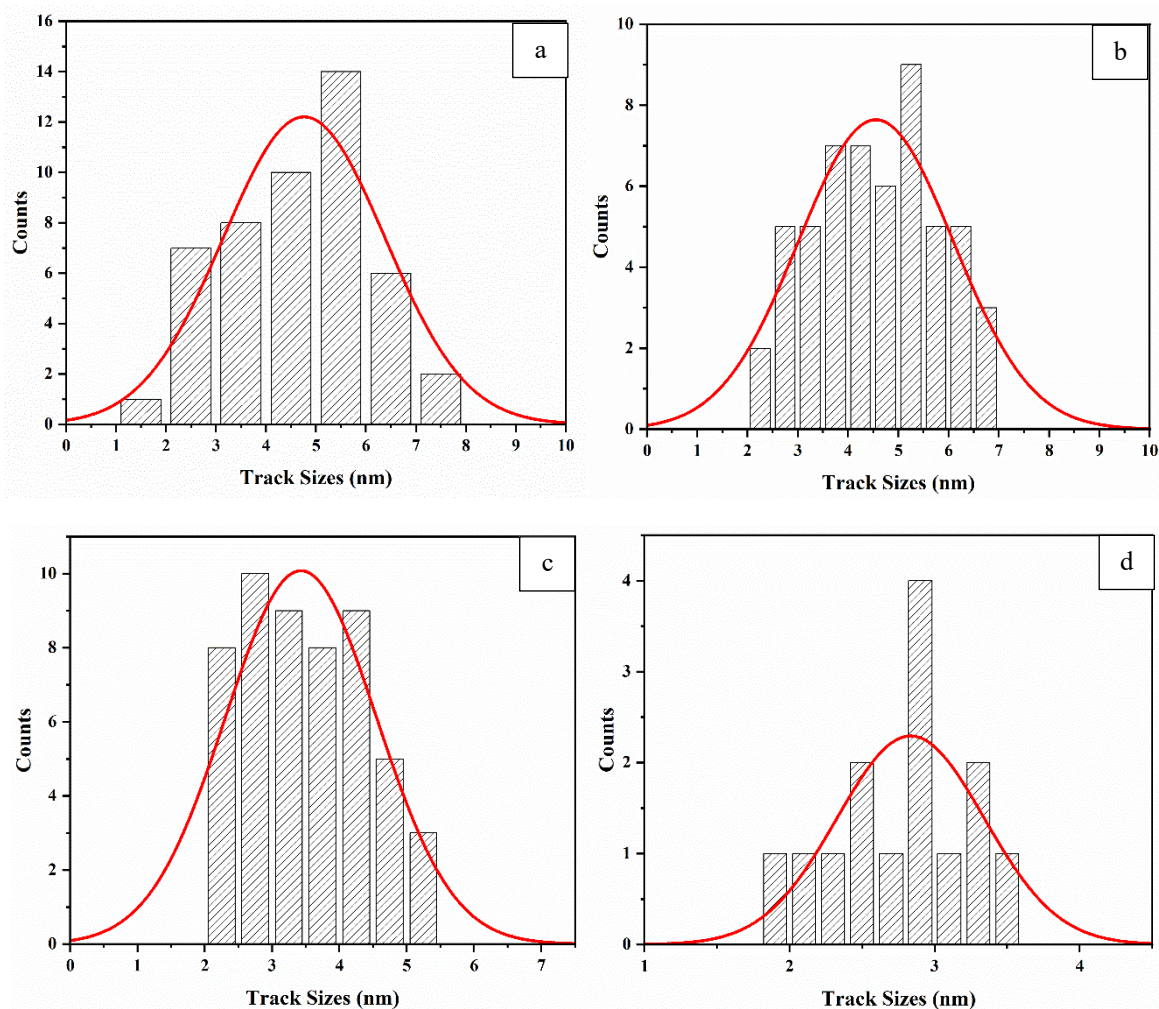


Fig. 10. The histograms of the track diameters with high standard deviation for nc-CeO₂ irradiated with 714 MeV Bi ions to a fluence of $5 \times 10^{11} \text{ cm}^{-2}$ with (a) 14 μm , (b) 17 μm , and (c) 19 μm Al degraders as well as for 148 MeV Xe ions with (d) 13 μm Al degrader. The size distributions were fitted with Gaussian as indicated by the dotted line.

The standard deviations were observed for 714 MeV Bi ions with degraders of thickness $17.40 \pm 0.19 \mu\text{m}$ and $19.16 \pm 0.27 \mu\text{m}$, 1.54 nm and 1.12 nm respectively. Whereas, the standard deviation for 148 MeV Xe ions with $13.66 \pm 0.12 \mu\text{m}$ degrader thickness was determined to be 0.51 nm. This implies that the measurements were not accurate and could be due to the over-estimation of the track diameters through direct observation in TEM analysis [24]. The track diameters in these specific irradiations were challenging to measure accurately due to poor contrast and track overlap in the TEM images, leading to higher standard deviations. The histograms for the other irradiation cases were not included, but the results were summarised.

The S_e values were determined through SRIM-2016 with the density for CeO₂ to be 7.13 g/cm^3 . Table 2 summarises the results for the track measurements as well as the details of the irradiation parameters obtained through TEM analysis.

The S_e values were determined through SRIM-2016 with the density for CeO_2 to be 7.13 g/cm^3 . Table 2 summarises the results for the track measurements as well as the details of the irradiation parameters obtained through TEM analysis.

Table 2

Summary of irradiation parameters, calculated electronic stopping powers with 2σ for 95 % confidence interval and extracted track parameters for nanocrystalline CeO_2

Ion and Initial Energy (MeV)	Al Degradar Thickness (μm)	Ion Energy (MeV/amu)	Average $S_e \pm 2\sigma$ (keV/nm)	Mean (nm)	Standard Deviation (nm)	Min (nm)	Max (nm)	# of Tracks Measured
Bi, 714	None	3.41	45.11	5.54	1.50	2.23	8.55	50
	14.03 ± 0.14	1.71 ± 0.02	38.58 ± 0.10	4.72	1.62	1.73	7.99	48
	17.40 ± 0.19	1.35 ± 0.02	35.60 ± 0.19	4.58	1.54	2.28	7.00	54
	19.16 ± 0.27	1.17 ± 0.02	33.74 ± 0.26	3.51	1.12	2.02	5.22	52
	23.24 ± 0.22	0.80 ± 0.01	28.51 ± 0.22	3.64	1.16	1.52	6.40	70
	26.98 ± 0.27	0.52 ± 0.02	22.58 ± 0.53	2.55	0.75	1.28	5.77	126
Xe, 220	None	1.66	27.66	2.82	0.99	0.95	5.43	64
Xe, 167	None	1.26	25.65	2.78	0.84	1.22	6.34	108
	9.05 ± 0.15	0.37 ± 0.01	15.63 ± 0.23	2.63	0.56	1.40	5.35	77
	11.74 ± 0.25	0.21 ± 0.01	11.10 ± 0.45	2.03	0.47	1.19	5.11	52
Xe, 156	None	1.18	25.12	3.16	0.90	2.14	5.68	91
	8.02 ± 0.17	0.40 ± 0.01	16.11 ± 0.26	2.53	0.52	1.69	6.02	123
	9.58 ± 0.19	0.29 ± 0.01	13.62 ± 0.31	2.79	0.86	1.38	5.40	89
Xe, 148	11.74 ± 0.25	0.15 ± 0.01	8.76 ± 0.46	2.61	0.68	1.77	4.62	29
	13.66 ± 0.12	0.07 ± 0.004	5.32 ± 0.20	2.21	0.51	1.86	3.42	14
Kr, 100	None	1.19	21.45	2.64	0.87	1.21	5.75	231
	8.02 ± 0.17	0.34 ± 0.01	11.23 ± 0.23	2.61	0.75	1.19	4.70	209
	9.58 ± 0.19	0.22 ± 0.01	8.98 ± 0.31	2.35	0.75	0.87	6.86	75
	11.74 ± 0.25	0.11 ± 0.01	5.38 ± 0.42	2.63	0.92	1.36	4.96	42

Some data values were excluded from Table 2 such as the Al degrader thickness of $28.74 \pm 0.43 \mu\text{m}$ ($S_e = 19.73 \pm 0.65 \text{ keV/nm}$) for 714 MeV Bi ions as they were deemed inaccurate due to poor contrast, and contamination. No tracks were visible for the Al degrader thickness of $16.04 \pm 0.24 \mu\text{m}$ ($S_e = 1.63 \pm 0.34 \text{ keV/nm}$) of 148 MeV Xe ions.. The data tabulated in Table 2 for the 220 MeV Xe ions were to a fluence of $5 \times 10^{11} \text{ cm}^{-2}$. The average track diameter and its respective standard deviation for the same ion and energy but to a fluence of $1 \times 10^{11} \text{ cm}^{-2}$ were determined to be $3.25 \pm 0.28 \text{ keV/nm}$. Similarly, for 714 MeV Bi ions, the data in Table 2 is for $5 \times 10^{11} \text{ cm}^{-2}$, hence the average track diameter and standard deviation to a fluence of $2 \times 10^{11} \text{ cm}^{-2}$ was determined to be $5.68 \pm 1.49 \text{ keV/nm}$.

The relationship between the determined S_e values and the extracted average track diameters were graphically represented in Fig. 11.

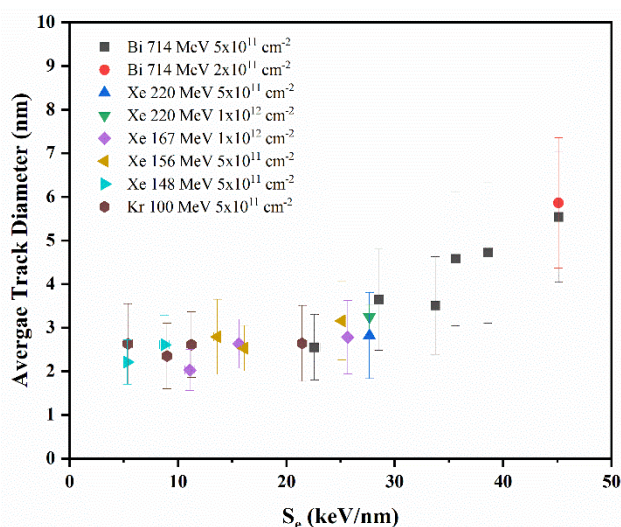


Fig. 11. The graphical representation of the dependence of the average track diameter on the electronic stopping power in irradiated nanocrystalline CeO_2 specimens with and without Al degraders

The average track diameter as a function of electronic stopping power for the various irradiation conditions is shown in Fig. 11. Each case illustrates an increase as a function of electronic stopping power. The experimental data for 714 MeV Bi ions to a fluence of $5 \times 10^{11} \text{ cm}^{-2}$, exhibits large error bars in the y-direction, indicating significant uncertainty in the measurements.

5. Conclusion

TEM analysis in conjunction with ImageJ and OriginPro software can be employed to directly measure the average track diameters induced by high energy Xe and Bi ions in nc-YIG and - CeO_2 . The ion tracks in nc-YIG by various ions and energies were observed as amorphous. In contrast the ion tracks in nc- CeO_2 were perceived to retain its crystallinity due to its resistance to structural modification by SHI irradiation. These observations are aligned with previous investigations. The ion tracks formed in nc-YIG and - CeO_2 at stopping powers in the range of 6.92 to 41.19 keV/nm and 5.32 to 45.11 keV/nm respectively, were observed. There was an increase in the track diameter measurements when the S_e values increased. The unirradiated nc- CeO_2 nanoparticles were observed to exhibit morphologies of cubic geometry. After irradiation, the edges of the particles appeared more rounded, possibly due to the presence of surface hillocks. At high fluences such as $5 \times 10^{12} \text{ cm}^{-2}$, track overlaps were observed and the nanoparticles appeared to transform into an amorphous material. The thresholding technique was applied to establish the nanoparticle areas in nc-YIG where tracks were measured. The particle size should have an effect on the size and nature of SHI-induced defects. However, due to inconsistent track contrast and associated measurement uncertainty in this investigation, the above could not be unambiguously verified. There is also a limited number of studies relating to how the grain size and nanocrystallinity affect the radiation response. As mentioned throughout this study, the results obtained for nc-YIG were from a reduced data set. Hence the sampling quality of the data was verified through the graphical relationship between the number of tracks and the particle area. Understanding the specific mechanisms of SHI-induced damage is crucial for the development and selection of inert matrix fuel hosts in nuclear applications as well as to investigate the responses of different materials to radiation damage. Therefore, future ion irradiation

studies should devote their resources to examine the responses of nanocrystal YIG and CeO₂ specimens under various radiation conditions.

6. Acknowledgements

I want to thank Dr. V. A. Skuratov and Dr. J. H. O'Connell for their guidance and for this immense opportunity to improve my knowledge and skills as a scientist and researcher. I have learned so much and I have no words to describe their patience and continuous support throughout this project. Furthermore, I highly appreciate the constructive feedback and insights from Dr. A. Mutali and Dr. R. A. Rymzhanov to navigate the challenges and complexities. I also want to thank the administration and START team members for their financial support and kindness. They always made time to assist and provide guidance. Visiting JINR was an excellent opportunity and I will treasure all the life lessons and use the knowledge for my future endeavours. Last but not least I want to thank the team at CHRTEM, South Africa, as well as my family and friends who supported, motivated and guided me to participate in the START Summer Program. I am forever grateful.

References

- [1] S. Sadekin, S. Zaman, M. Mahfuz, and R. Sarkar, "Nuclear power as foundation of a clean energy future: A review," *Energy Procedia*, vol. 160, pp. 513–518, Feb. 2019, doi: 10.1016/j.egypro.2019.02.200.
- [2] S. J. Zinkle and G. S. Was, "Materials challenges in nuclear energy," *Acta Materialia*, vol. 61, no. 3, pp. 735–758, Feb. 2013, doi: 10.1016/j.actamat.2012.11.004.
- [3] G. S. Was, D. Petti, S. Ukai, and S. Zinkle, "Materials for future nuclear energy systems," *Journal of Nuclear Materials*, vol. 527, p. 151837, Dec. 2019, doi: 10.1016/j.jnucmat.2019.151837.
- [4] G. S. Was, "Introduction" in *Fundamentals of Radiation Materials Science: Metals and Alloys*, 2nd ed. New York: Springer, 2016, pp. xxiii–xxvii.
- [5] M. Lang, F. Djurabekova, N. Medvedev, M. Toulemonde, and C. Trautmann, "1.15 - Fundamental Phenomena and Applications of Swift Heavy Ion Irradiations," *Comprehensive Nuclear Materials (Second Edition)*, vol. 1, pp. 485–516, Jan. 2020, doi: 10.1016/B978-0-12-803581-8.11644-3.
- [6] A.I. Ryabchikov, "Progress in low energy high intensity ion implantation method development," *Surface & Coatings Technology*, vol. 388, pp. 125561–125561, Apr. 2020, doi: 10.1016/j.surfcoat.2020.125561.
- [7] L. Thomé, S. Moll, A. Debelle, F. Garrido, G. Sattonnay, and J. Jagielski, "Radiation Effects in Nuclear Ceramics," *Advances in Materials Science and Engineering*, vol. 2012, pp. 1–13, Jan. 2012, doi: 10.1155/2012/905474.
- [8] R.A. Rymzhanov *et al.*, "Insights into different stages of formation of swift heavy ion tracks," *Nuclear Instruments and Methods in Physics Research Section B: Beam Interactions with Materials and Atoms*, vol. 473, pp. 27–42, Jun. 2020, doi: 10.1016/j.nimb.2020.04.005.
- [9] M. Toulemonde, C. Dufour, A. Meftah, and E. Paumier, "Transient thermal processes in heavy ion irradiation of crystalline inorganic insulators," *Nuclear Instruments and Methods in Physics*

- Research Section B: Beam Interactions with Materials and Atoms*, vol. 166–167, pp. 903–912, May 2000, doi: 10.1016/s0168-583x(99)00799-5.
- [10] H. Matzke, “INERT MATRIX FUELS TO REDUCE THE RADIOTOXICITY OF NUCLEAR WASTE,” in *Proceedings of the AATN '99: 26th Annual Meeting of the Argentine Association of Nuclear Technology*, Buenos Aires, Argentina: Asociacion Argentina de Tecnologia Nuclear (AATN), Jul. 1999, pp. 1–10
- [11] W. F. Cureton, C. L. Tracy, and M. Lang, “Review of Swift Heavy Ion Irradiation Effects in CeO₂,” *Quantum Beam Science*, vol. 5, no. 2, p. 19, Jun. 2021, doi: <https://doi.org/10.3390/qubs5020019>.
- [12] K. Yasuda *et al.*, “Defect formation and accumulation in CeO₂ irradiated with swift heavy ions,” *Nuclear Instruments and Methods in Physics Research Section B: Beam Interactions with Materials and Atoms*, vol. 314, pp. 185–190, Nov. 2013, doi: 10.1016/j.nimb.2013.04.069.
- [13] J.-M. Costantini, J. M. Desvignes, and M. Toulemonde, “Amorphization and recrystallization of yttrium iron garnet under swift heavy ion beams,” *Journal of Applied Physics*, vol. 87, no. 9, pp. 4164–4174, May 2000, doi: 10.1063/1.373047.
- [14] A. Ibrayeva *et al.*, “Swift heavy ion tracks in nanocrystalline Y₄Al₂O₉,” *Nuclear Materials and Energy*, vol. 30, p. 101106, Mar. 2022, doi: 10.1016/j.nme.2021.101106.
- [15] A. Janse van Vuuren *et al.*, “Latent tracks of swift Bi ions in Si₃N₄,” *Materials Research Express*, vol. 7, no. 2, p. 025512, Feb. 2020, doi: 10.1088/2053-1591/ab72d3.
- [16] A. Janse van Vuuren *et al.*, “High-energy heavy ion tracks in nanocrystalline silicon nitride,” *Crystals*, vol. 12, no. 10, p. 1410, Oct. 2022. doi:10.3390/cryst12101410.
- [17] S. Tavernier, “1.4 Probability and Statistics,” in *Experimental Techniques in Nuclear and Particle Physics*, Berlin, Heidelberg: Springer Berlin Heidelberg, 2010, pp. 7–9
- [18] A. Ibrayeva, J. O’Connell, A. Mutali, R. Rymzhanov, and V. Skuratov, “Transmission Electron Microscopy and Molecular Dynamic Study of ion tracks in nanocrystalline Y₂Ti₂O₇: Particle size effect on track formation Threshold,” *Crystals*, vol. 13, no. 11, p. 1534, Oct. 2023, doi: 10.3390/cryst13111534.
- [19] M. M. Saifulin, J. H. O’Connell, A. J. Van Vuuren, V. A. Skuratov, N. S. Kirilkin, and M. V. Zdorovets, “Latent tracks in bulk yttrium-iron garnet crystals irradiated with low and high velocity krypton and xenon ions,” *Nuclear Instruments and Methods in Physics Research Section B Beam Interactions With Materials and Atoms*, vol. 460, pp. 98–103, Dec. 2019, doi: 10.1016/j.nimb.2018.11.023.
- [20] J. Jensen, A. Dunlop, S. Della-Negra, and M. Toulemonde, “A comparison between tracks created by high energy mono-atomic and cluster ions in Y₃Fe₅O₁₂,” *Nuclear Instruments and Methods in Physics Research Section B Beam Interactions With Materials and Atoms*, vol. 146, no. 1–4, pp. 412–419, Dec. 1998, doi: 10.1016/s0168-583x(98)00442-x.

- [21] I. Florea, C. Féral-Martin, J. Majimel, D. Ihiawakrim, C. Hirlimann, and O. Ersen, “Three-Dimensional tomographic analyses of CeO₂ nanoparticles,” *Crystal Growth & Design*, vol. 13, no. 3, pp. 1110–1121, Feb. 2013, doi: 10.1021/cg301445h.
- [22] S. Takaki, K. Yasuda, T. Yamamoto, S. Matsumura, and N. Ishikawa, “Atomic structure of ion tracks in Ceria,” *Nuclear Instruments and Methods in Physics Research Section B: Beam Interactions With Materials and Atoms*, vol. 326, pp. 140–144, May 2014, doi: 10.1016/j.nimb.2013.10.077.
- [23] N. Ishikawa *et al.*, “Study of structural change in CeO₂ irradiated with high-energy ions by means of X-ray diffraction measurement,” *Nuclear Instruments and Methods in Physics Research Section B Beam Interactions With Materials and Atoms*, vol. 266, no. 12–13, pp. 3033–3036, Jun. 2008, doi: 10.1016/j.nimb.2008.03.159.
- [24] J. O’Connell, V. Skuratov, A. J. Van Vuuren, M. Saifulin, and A. Akilbekov, “Near surface latent track morphology of SHI irradiated TiO₂,” *Physica Status Solidi (B)*, vol. 253, no. 11, pp. 2144–2149, Aug. 2016, doi: 10.1002/pssb.201600473.